Research Article Vol. 33, No. 14 / 14 Jul 2025 / Optics Express 30441
Optics EXPRESS

High-efficiency and eco-friendly Cs_2SnBr_6-based perovskite solar cells: optimized device architecture and performance analysis via SCAPS-1D simulation

MD. SELIM REZA,[1] AVIJIT GHOSH,[1,*] YEDLURI ANIL KUMAR,[2] MD AL IMRAN,[3] KHORSHED ALAM,[4] MD MAHFUZUR RAHMAN,[5] NASSER S. AWWAD,[6] AND HALA A. IBRAHIUM[7]

[1]*Department of Electrical and Electronic Engineering, Begum Rokeya University, Rangpur-5400, Bangladesh*
[2]*Saveetha School of Engineering, Saveetha Institute of Medical and Technical Sciences, SIMATS, Chennai, India*
[3]*Department of Electrical and Computer Engineering, Lamar University, Beaumont, Texas 77710, USA*
[4]*Department of Industrial and Systems Engineering, Lamar University, Beaumont, Texas 77710, USA*
[5]*Department of Electrical and Electronic Engineering, Uttara University, Holding 77 Beribadh Road, Dhaka 1230, Bangladesh*
[6]*Department of Chemistry, King Khalid University, Al Qura'a, Abha, P.O. Box 960, Saudi Arabia*
[7]*Department of Biology, King Khalid University, Al Qura'a, Abha, P.O. Box 960, Saudi Arabia*
[*]*avijitghosheee@gmail.com*

Abstract: This study aims to develop a sustainable, high-efficiency Cs_2SnBr_6-based perovskite solar cell (PSC) while eliminating the use of hazardous materials. The proposed device architecture Al/FTO/CdS/Cs_2SnBr_6/CBTS/Ni (Device I) demonstrates an enhanced fill factor (FF) and an impressive power conversion efficiency (PCE). Key performance variables like perovskite layer depth, defect density, and the effects of series and shunt resistances are critically evaluated. Comparative analysis of various hole transport layers (HTLs: CBTS, P_3HT, and CuO) and electron transport layers (ETLs: CdS, SnO_2, and ZnSe) identifies CdS and CBTS as the most effective materials for achieving optimal performance. Simulation results obtained using SCAPS-1D reveal that Device I can achieve a short-circuit current density (J_{SC}) of 33.084 mA/cm^2, an open-circuit voltage (V_{OC}) of 1.111 V, an FF of 88.82%, and a PCE of 32.65% under AM 1.5 solar illumination, with a perovskite thickness of 1.0 µm and ETL/HTL thicknesses of 0.05 µm. Devices II and III recorded PCEs of 30.59% and 23.25%, respectively. In addition, quantum efficiency (QE), carrier dynamics, and temperature effects were thoroughly analyzed. Device I demonstrated significant potential for the development of high-efficiency, fully inorganic Cs_2SnBr_6-based PSCs. The findings support the viability of Cs_2SnBr_6 as a sustainable and environmentally friendly material for next-generation solar energy technologies.

1. Introduction

The rising global demand for electricity, along with the environmental, economic, and logistical drawbacks of non-renewable energy, has driven the urgent search for clean, sustainable alternatives. Fossil fuel emissions remain a key contributor to climate change, emphasizing the need for reliable renewable energy sources [1,2]. The increasing global demand for electricity is driving scientists to explore alternatives to conventional energy sources. At the same time, the limited availability of non-renewable resources along with their harmful environmental impact, high costs, and significant logistical challenges has intensified the need for clean, sustainable energy solutions [2,3]. Due to silicon's indirect bandgap and high production cost, the performance

#566116 https://doi.org/10.1364/OE.566116
Journal © 2025 Received 24 Apr 2025; revised 17 Jun 2025; accepted 17 Jun 2025; published 10 Jul 2025

Optics EXPRESS

of conventional solar cells was initially low [4]. Since 2009, certain hybrid inorganic–organic lead halide (OILHP) compounds have demonstrated significant potential as materials for solar cell applications. Their outstanding properties have garnered considerable attention for their suitability in solar energy conversion. Key advantages include high power conversion efficiency (PCE), an optimal bandgap, excellent charge carrier mobility, a high absorption coefficient, and strong resistance to defects [4–6].

Solar cells have become a feasible alternative for sustainable energy production in response to these environmental issues. Solar technology has advanced significantly during the last ten years, and PCE has steadily increased. For example, in 2009, PSC efficiency was only 3.8% [7]. PSCs are one of the third-generation photovoltaic technologies that have garnered a lot of attention because of their cost and great efficiency [8]. Perovskite solar cells (PSCs) have greatly benefited from simulation software modeling tools like SCAPS-1D, which allow for the modeling and improvement of PV model designs before physical fabrication. This approach helps minimize substance scrap and reduce manufacturing costs [9,10]. SCs transform light energy into photovoltaic energy by reacting distinctly to various optical wavelengths [10]. Scholars using quantitative simulations have recently achieved noteworthy findings, surpassing earlier benchmarks [11]. The usage of SCAPS-1D simulation software facilitates the validation of theory through experiment analysis outcomes. However, the need for environmentally friendly materials remains a significant challenge in their development. Despite the well-documented toxic effects of lead on human health and the environment, it has been widely used in many perovskite structures [12]. Exposure to lead can cause serious health problems, such as harm to the cardiovascular, immunological, reproductive, and kidney systems [13]. Additionally, lead poisoning can impair the blood's oxygen-carrying capacity and, at high concentrations, adversely affect reproductive function in animals [14]. As a result, lead presents a major obstacle to using PSCs to provide clean and sustainable energy solutions. Lead must be eliminated from PSCs' composition in order to address the issue of toxicity. The primary difficulty is to develop a lead-free substitute that is both economical and effective while maintaining good performance. Numerous lead-free perovskite solar cells have been modeled recently, showing promising results in important performance parameters such as PCE, V_{OC}, J_{SC}, and FF [15–18]. X_2SnBr_6 belongs to the X_2BA_6 family of compounds, where **X** represents monovalent cations such as Cs^+, Rb^+, K^+, and Na^+; **B** denotes divalent cations like Si^{2+}, Ge^{2+}, Sn^{2+}, and Pb^{2+} [19]; and **A** stands for halide anions including F^-, Cl^-, Br^-, and I^-. X_2SnBr_6, in particular, exhibits a high-symmetry crystal structure analogous to cubic halide perovskites and crystallizes in the $Fm3^-m$ space group, which contributes to its favorable optoelectronic properties [20–22].To evaluate the overall performance of dual-absorber solar cells (SCs), a comprehensive investigation was conducted using various electron transport layers (ETLs) such as cadmium sulfide (CdS), tin(IV) oxide (SnO_2), and zinc selenide (ZnSe), along with different hole transport layers (HTLs) including copper(II) oxide (CuO), poly(3-hexylthiophene) (P_3HT), and copper barium tin sulfide (CBTS). These materials were selected based on their ability to facilitate effective charge transport and reduce recombination losses. In addition to material selection, several critical device parameters were optimized, including operating temperature, defect density within the active layer, series and shunt resistance, and the thicknesses of the absorber and transport layers. These factors were found to significantly influence the device's power conversion efficiency (PCE) and overall stability. The most efficient configuration employed the lead-free perovskite absorber Cs_2SnBr_6, which exhibited a band gap of 1.358 eV and achieved an impressive PCE of 32.65%. This result underscores the potential of environmentally friendly, high-efficiency perovskite solar cells. The simulation outcomes are expected to provide valuable guidance for future experimental research and practical development in the field of photovoltaics. Additionally, three device architectures were proposed to explore the impact of different HTLs, designated as Device I (Al/FTO/CdS/Cs_2SnBr_6/CBTS/Ni), Device II (Al/FTO/CdS/Cs_2SnBr_6 /P_3HT/Ni), and

Optics EXPRESS

Device III (Al/FTO/CdS/Cs_2SnBr_6/CuO/Ni), enabling a comparative analysis of their respective performances.

In this study, a novel device architecture, Al/FTO/CdS/Cs_2SnBr_6/CBTS/Ni, is proposed to overcome the limitations of conventional perovskite solar cells (PSCs). In this configuration, aluminum (Al) and nickel (Ni) serve as the front and rear metal contacts, with work functions of 4.20 eV and 5.22 eV, respectively. The transparent conductive oxide (TCO) layer is composed of fluorine-doped tin oxide (FTO) or indium tin oxide (ITO), ensuring efficient light transmission and electrical conductivity. Cadmium sulfide (CdS) is employed as the electron transport layer (ETL) due to its high absorption coefficient, appropriate bandgap, excellent carrier mobility, and strong electrical conductivity, allowing it to form an effective interface with the Cs_2SnBr_6 absorber layer and facilitate efficient charge transport [23]. Abdelaziz et al. [24] investigated the influence of CZTS and MoS_2 layer thicknesses, charge carrier concentration, and bottom metal contact on the performance of CZTS-based solar cells. Their study combined theoretical analysis with experimental validation of the Al-ZnO/CdS/CZTS/MoS_2/Mo structure using SCAPS-1D simulation software. Similarly, Rahul et al. [25] designed and simulated a previously reported heterostructure (SLG/Mo/SnSe/CdS/i-ZnO/AZO/Al) using the SCAPS-1D program to analyze its photovoltaic performance. Cs_2SnBr_6 has been identified as a promising lead-free perovskite material, exhibiting favorable structural and electronic characteristics [26]. Initial research on K_2SnBr_6-based perovskites reported a relatively low PCE of 27.25%. However, further developments using Rb_2SnBr_6 resulted in a significantly improved peak efficiency of 30.32% [26]. Highlighting the promise of tin-based perovskites, this study also emphasizes the crucial impact of the hole transport layer (HTL) in ensuring device stability. CBTS stands out as a cost-effective and easily processable organic HTL, offering high hole mobility and excellent long-term stability. Although materials like CuO and P_3HT have demonstrated strong performance, their high cost remains a major barrier to widespread commercial adoption. As a result, this work identifies Cs_2SnBr_6 and CBTS as promising candidates for the advancement of efficient, stable, and lead-free hybrid perovskite SCs.

2. Architecture and parameters

2.1. Approach to simulation

SCAPS-1D, a modeling tool developed by Professor Marc Burgelman, was selected for this study due to its advantages over other simulation programs and its proven reliability in producing results consistent with previous research [27]. A comprehensive understanding of the fundamental physics underlying SCAPS (solar cell capacitance simulator) requires an in-depth examination of the one-dimensional semiconductor equations. These include the transit equation, the continuity equation, and Poisson's equation, all of which must be considered alongside various recombination mechanisms. The continuity equation defines the relationship between charge carrier generation, recombination, and transport, specifically for electrons and holes. The transit formula portrays the motion of these charges within the solar cell, governed by both drift due to electric fields and diffusion resulting from concentration gradients. Poisson's equation, on the other hand, determines the spatial variation of electrostatic potential based on charge distribution and the internal electric field. Key physical parameters in this context include diffusivity, which quantifies how efficiently charge carriers spread through the material, and diffusion length, which represents the average distance a carrier travels before recombining. The carrier lifetime denotes the average duration a charge carrier exists before undergoing recombination, directly influencing the efficiency of carrier collection. The V_{OC} indicates the maximum voltage across the electrode contacts of an SC (solar cell) in the absence of an external electrical load. To accurately model and analyze a solar cell structure, it is necessary to solve a set of fundamental equations (1) through (7). SCAPS provides robust numerical solutions to these equations, allowing for the precise simulation of photovoltaic parameters and serving as a powerful tool for solar cell analysis

Optics EXPRESS

and optimization.

$$\text{Poisson Equations:} \quad \frac{\partial^2 \varphi}{\partial x^2} = -\frac{\partial E}{\partial x} = -\frac{\rho}{\varepsilon_s} = -\frac{q}{\varepsilon_s}[p - n + N_D(x) - N_A(x) \ \pm N_{\text{def}(x)}] \tag{1}$$

$$\text{Continuity Equations:} \quad \frac{\partial_{n.p}}{\partial x} = \frac{1}{q}\frac{\partial J_n}{\partial x} + (G_n - R_n) + \frac{1}{q}\frac{\partial J_p}{\partial x} + (G_p - R_p) \tag{2}$$

$$\text{Transport Equations:} \quad J_{n.p} = nq\mu_n E + qDn\frac{\partial n}{\partial x} + pq\mu_p E + qDp\frac{\partial p}{\partial x} \tag{3}$$

$$\text{Diffusivity:} \quad D_{n.p} = \left[\left(\frac{k_B T}{q}\right)\mu_{n.p}\right] \tag{4}$$

$$\text{Diffusion length:} \quad L_{n.p} = \sqrt{D_{n.p}\tau_{n.p}} \tag{5}$$

$$\text{Open circuit voltage:} \quad V_{OC} = \frac{nk_B T}{q}\left[\ln\left(\frac{I_L}{I_0} + 1\right)\right] \tag{6}$$

$$\text{Carrier lifetime:} \quad \tau = \frac{1}{\sigma N_t v_{th}} \tag{7}$$

In this context, φ denotes the electrostatic potential within the solar cell, while **ε** represents the material's permittivity, and E corresponds to the electric field. The variables n and p refer to the concentrations of free electrons and holes, respectively. N_D and N_A show the donor and acceptor dopant concentrations, whereas N_{def} represents the density of possible defect states. The symbols p and q denote charge density and the elementary charge, respectively. μ_n, p signifies the mobility of electrons (n) or holes (p). The term $G_{n,p}$ refers to the optical generation rate of charge carriers, and $\tau_{n,p}$ indicates the carrier lifetime for electrons or holes. The expression $\frac{\partial_{n.p}}{\partial x}$ represents the spatial concentration gradient of electrons or holes, while $R_{n,p}$ denotes their recombination rate [28].

2.2. Design arrangement

Figure 1(a) illustrates the diagram design of the primary model, which incorporates a sodium (Na)-based perovskite solar cell (PSC). This architecture follows an n-i-p configuration, consisting of a front contact, back contact, and an electron transport layer (ETL), along with a Cs_2SnBr_6 absorber layer. In this n-i-p structure, the depletion region extends deeply into the intrinsic layer of the device. This extended depletion zone enhances the cell's sensitivity to long-wavelength photons, which are capable of penetrating further into the absorber. However, efficient charge generation primarily occurs for electron-hole pairs formed within or near the depletion region. A broader depletion zone thus improves quantum efficiency by facilitating the effective separation and collection of these charge carriers. The hetero-structural nature of Cs_2SnBr_6 supports strong light absorption and ensures efficient charge confinement and photon management. Additionally, heavily doped layers at the ETL and HTL interfaces promote the formation of ohmic contacts.

In this configuration, nickel (Ni) serves as the back metal contact (BMC), while fluorine-doped tin oxide (FTO) is used as the right contact. Several materials, such as CdS, SnO_2, and ZnSe, are explored as candidate ETLs. The band gap dynamics of the Al/FTO/CdS/Cs_2SnBr_6/Ni structure are presented in Fig. 1(b). Simulation parameters for the perovskite layer, ETLs, and HTLs (considered for further analysis) are compiled in Table 1, while Table 2 outlines the interfacial defect parameters. Simulations were performed under standard AM1.5G solar illumination, with an irradiance of 1000 W/m^2, a temperature of 300 K, and an operating frequency of 1 MHz. The electrical parameters for the models were derived through computational simulations, with Table 1 presenting detailed values for three electron transport layers (ETLs) and the FTO

Optics EXPRESS

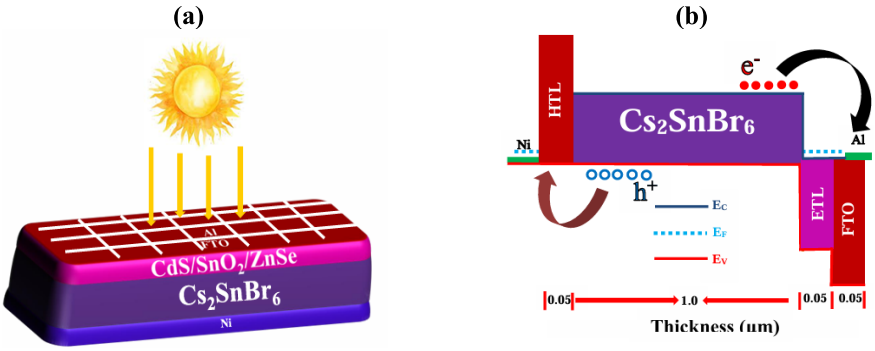

Fig. 1. (a) Architectre structure and (b) arrangement of bands of Al/FTO/CdS/Cs_2SnBr_6/Ni PV cell.

Table 1. Simulation settings for the ETL layer and FTO in SCAPS-1D

Parameters	FTO [29]	CdS [30]	SnO_2 [19]	ZnSe [31]
t(nm)	50	50	50	50
E_g (eV)	3.6	2.4	3.6	1.8
χ (eV)	4.5	4.2	4	4.55
ε_r	10	10	9	5.54
N_C (cm^{-3})	2×10^{18}	2.2×10^{18}	2.2×10^{18}	1×10^{18}
N_t (cm^{-3})	1×10^{14}	1×10^{13}	1×10^{14}	1×10^{14}
μ_n (cm^2/(Vs))	100	100	100	100
μ_h (cm^2/(Vs))	20	25	25	50
N_D (cm^{-3})	1×10^{18}	1×10^{19}	1×10^{16}	1×10^{18}
N_A (cm^{-3})	0	0	0	0
N_V (cm^{-3})	1.8×10^{19}	1.8×10^{19}	1.8×10^{19}	1×10^{18}

Table 2. The absorber and HTL layer parameters are summarized

Parameters	CBTS [19]	CuO [19]	P_3HT [19]	Cs_2SnBr_6 [26]
t(nm)	50	50	50	1000
E_g (eV)	1.9	1.51	1.7	1.358
χ (eV)	3.6	4.07	3.5	4.09
(relative, ε_r)	5.4	18.1	3	4.00
N_C (cm^{-3})	2.2×10^{18}	2.2×10^{19}	2×10^{21}	1.955×10^{18}
N_t (cm^{-3})	10^{14}	10^{14}	10^{14}	10^{14}
μ_n (cm^2/(Vs))	30	100	0.0018	250
μ_h (cm^2/(Vs))	10	10	0.0186	100
N_D (cm^{-3})	0	0	0	0
N_A (cm^{-3})	10^{18}	10^{18}	10^{18}	10^{18}
N_V (cm^{-3})	1.8×10^{19}	5.5×10^{20}	2×10^{21}	1.401×10^{19}

Optics EXPRESS

front contact, while Table 2 sketches the corresponding criteria for the HTLs and the Cs_2SnBr_6 absorber.

These parameters include level thickness (t), electron affinity (χ), relative dielectric constant (ε_r), bandgap energy (E_g), electron and hole mobilities (μ_n and μ_p), donor and acceptor doping concentrations (N_D and N_A), carrier density of states in the conduction and valence bands (N_C and N_V), and the overall defect density (N_t). Interface characteristics were also incorporated, with the reference energy level for defects set at 0.6 eV below the valence band maximum (E_V). The defects were modeled as single-level, neutral in nature, with electron and hole capture cross-sections of 10^{-19} cm^2 and 10^{-18} cm^2, respectively. A uniform defect density of 10^{10} cm^{-2} was assumed across all interfaces, including ETL/absorber and absorber/HTL junctions. This comprehensive parameter set is crucial for accurately evaluating the outcome of defect concentrations on model efficiency while maintaining consistency across all simulated configurations.

3. Results and discussion

3.1. Improvement of ETL

3.1.1. Effects of ETL depth on the device's operating efficacy and potential optimization paths

The ETL's thickness, which includes components like CdS, SnO_2, and ZnSe, is a critical factor affecting PSC efficiency. Improving the device's overall performance requires optimizing this setting. A well-chosen ETL can increase light transmission and significantly lower recombination currents, increasing efficiency [32]. In this experiment, the depth of the ETL was systematically diverse between 25 and 200 nm, while remaining factors were held constant, as detailed in Tables 1 and 2. Key performance indicators power conversion efficiency (PCE), short-circuit current density (J_{SC}), open-circuit voltage (V_{OC}), and fill factor (FF) are presented in Fig. 2, illustrating the control of ETL depth on device performance. The results indicate that even in the absence of a hole transport layer (HTL), these performance metrics remained largely stable. However, across all measured parameters, devices incorporating an HTL consistently outperformed those without one. Among the four ETL materials evaluated, a thickness of 50 nm for CdS yielded the highest efficiency, identifying it as the optimal thickness. Overall, variations in ETL thickness showed no significant impact on the performance of the perovskite solar cells (PSCs). As illustrated in Fig. 2, CdS outperformed the other ETL materials, exhibiting the highest power conversion efficiency (PCE). This choice not only enhances device performance but also contributes to reduced fabrication costs. Under optimal conditions, the PSC achieved a PCE of 22.54%, a V_{OC} of 0.9393 V, a J_{SC} of 27.605 mA/cm^2, and an FF of 86.91%.

3.1.2. Analysis of how differences in doping density and CdS ETL layer defects affect photovoltaic performance metrics

The selection of an appropriate ETL is critical to enhancing the performance of photovoltaic (PV) devices. The ETL plays a dual role: it facilitates the efficient extraction and transport of photogenerated electrons while simultaneously acting as a barrier to holes. This selective charge transport behavior effectively suppresses undesirable electron-hole recombination, thereby improving the total performance of the SC (solar cell). A well-optimized ETL not only ensures efficient charge separation and collection but also contributes significantly to key efficiency metrics, like PCE, V_{OC}, J_{SC}, and FF. In this study, cadmium sulfide (CdS) was selected and analyzed as the ETL material due to its favorable optoelectronic properties and compatibility with the absorber layer used in the proposed SC structure. To evaluate the influence of CdS ETL properties on device performance, we systematically investigated the effect of N_D and N_t on the operational parameters of the solar cell. The investigation was conducted by varying N_D within the range of 10^{13} to 10^{20} cm^{-3}, and N_t within the range of 10^{10} to 10^{16} cm^{-3}, while keeping all other parameters constant. Figure 3 illustrates the relationships between N_D and N_t and the

Optics EXPRESS

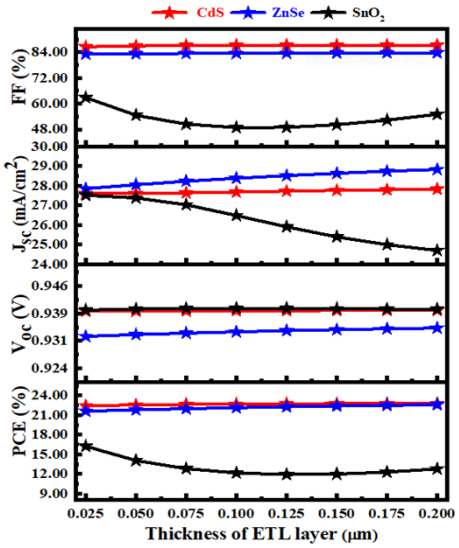

Fig. 2. The efficiency of ETL-layered solar cells with CdS, ZnSe, SnO_2

resulting solar cell efficiency measurements, specifically, PCE, V_{OC}, J_{SC}, and FF. As depicted in Figs. 3(a–d), when N_D is enhanced from 10^{13} to 10^{20} 1/cm^3 and N_t is varied from 10^{10} to 10^{16} 1/cm^3, the device performance metrics remain relatively stable. Under these conditions, the PCE, V_{OC}, J_{SC}, and FF were observed to remain around 22.39%, 0.939 V, 27.55 mA/cm^2, and 86.51%, respectively. This suggests that within this doping range, the ETL maintains optimal charge transport and minimal recombination, ensuring stable device operation. As N_D was further increased beyond 10^{16} to 10^{19} 1/cm^3, and N_t was increased beyond 10^{13} 1/cm^3, the device performance showed a slight improvement, reaching a maximum PCE of 22.77%. At this point, the other parameters were recorded as $V_{OC} = 0.939$ V, $J_{SC} = 27.91$ mA/cm^2, and FF = 86.82%, indicating an optimal doping condition. This performance enhancement can be attributed to improved conductivity and electron extraction efficiency at higher doping concentrations, without significantly increasing recombination losses. However, further increases in N_D beyond 10^{19} 1/cm^3 and N_t beyond 10^{13} 1/cm^3 resulted in a noticeable decline in all key performance indicators. This degradation is likely due to increased defect-related recombination and reduced carrier lifetime, which negatively affect charge transport and collection. Hence, over-doping the ETL can be detrimental to device performance, highlighting the importance of optimizing the doping levels to achieve maximum efficiency. Based on this analysis, the optimal doping concentrations for CdS as an ETL were determined to be $N_D = 10^{19}\,cm^{-3}$ and $N_t = 10^{13}\,cm^{-3}$, under which the maximum PCE of 22.77% was achieved. These findings confirm that CdS is a highly effective ETL for the proposed solar cell architecture and justify its selection for further optimization in subsequent phases of this research.

3.2. Band alignment modifications and sophisticated gadget design

As displayed in Fig. 4(a), this study examines a heterojunction SC employing Cs_2SnBr_6 as the light-absorbing material. The device architecture consists of three primary regions: the n-type layer (ETL), the intrinsic layer (active absorber), and the p-type layer (HTL). A mathematical analysis was conducted using three different hole transport layers: CBTS, P_3HT, and CuO. Aligned between the ETL and HTL, the Cs_2SnBr_6 layer performs as the primary absorber, generating excitons upon illumination. The ETL facilitates efficient electron transport while simultaneously acting as a barrier to suppress hole movement, thereby enhancing charge separation and reducing

Optics EXPRESS

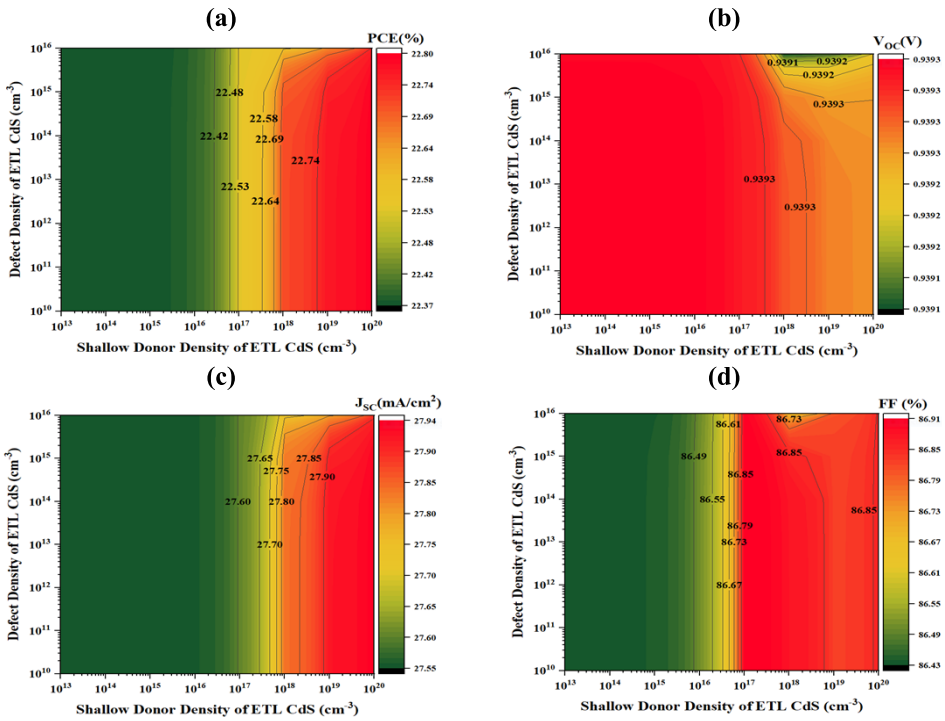

Fig. 3. Disparities between doping density and ETL fault about PV functioning aspects (a) PCE, (b) V_{OC}, (c) J_{SC}, (d) FF.

recombination. In contrast, electron flow is restricted at the HTL-absorber contact, thereby promoting efficient hole extraction. The inherent electric field's existence within the device is essential for the effective dissociation of excitons into free charge carriers. Figure 4(b) presents the energy band arrangement for the configuration of Al/FTO/CdS/Cs_2SnBr_6/HTL/Ni. Research has shown that nikel (Ni) possesses a work function greater than 5 eV [26]. In the solar cells structured as Al/FTO/CdS/Cs_2SnBr_6/(CBTS, P_3HT, and CuO)/Ni, this elevated Ni work function creates a Schottky barrier; this strongly enhances charge gathering and fits well with the CBTS valence band, thus enhancing hole transport. Because of this ideal band alignment, the solar cell's stability and efficiency are enhanced, electrical conductivity rises, and recombination losses decrease [33].

Key parameters like the depth of the absorber layer, doping concentrations, and defect density were optimized using advanced modeling techniques. Additionally, insights from existing literature were incorporated to enhance the material properties and structural attributes of each layer within the solar cell. The interface between the perovskite and the HTL was carefully engineered to function as a continuous tunneling junction, thereby minimizing electrical resistance and eliminating optical losses. Furthermore, the overall depth of the device was optimized based on the quarter-wavelength criterion, a method known to enhance light absorption while simultaneously reducing reflection losses, leading to improved overall efficiency. This theory states that phase opposition arises when the thickness of a layer is an odd multiple of λ/4, where λ is the wavelength of light in the medium. By reducing reflected light, this effect improves the efficiency of both absorption and transmission. For instance, solar penetration and clarity are enhanced when the FTO layer's depth is modified to λ/4 at key wavelengths between 500 and 700 nm. The CBTS ETL benefits from improved light transmission due to its lower reflectance. Meanwhile, the λ/4 optical thickness strategy is employed to enhance light absorption in the

Optics EXPRESS

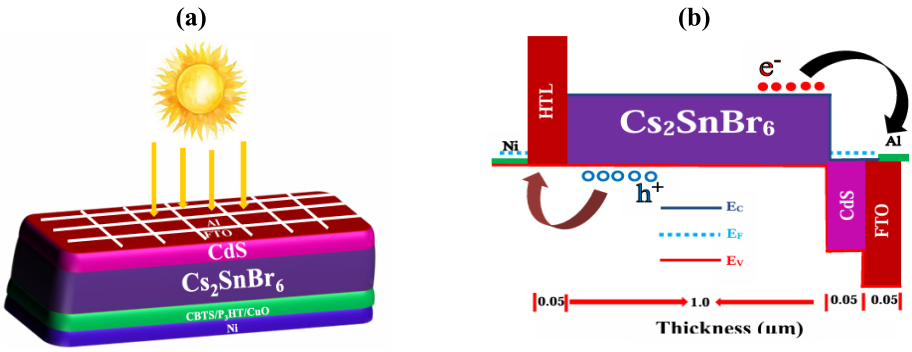

Fig. 4. Al/FTO/CdS/Cs_2SnBr_6/HTL/Ni schematic representation (a) and band configurations (b).

CBTS, P_3HT, and CuO layers by reducing reflection losses. However, practical manufacturing constraints must be considered during the implementation stage. To mitigate shunting effects and shield the upper layers from potential damage caused by sputtering or solvent exposure, a nonpolar recombination layer is incorporated between the perovskite levels. The electrical properties used for the HTL and absorber materials in this simulation-based optimization are summarized in Table 2, based on data from relevant experimental and computational studies.

3.3. *Diagram of the band*

Figures 5(a–c) illustrate the optimized energy band diagrams of the perovskite solar cells (PSCs) employing cesium tin (IV) bromide (Cs_2SnBr_6) as the absorber layer. The valence and conduction band offsets, which represent the energy level differences between the absorber layer and adjacent transport layers, are significantly influenced by the choice of ETL. In this configuration, Cs_2SnBr_6 serves as the absorber, while copper barium thiostannate (CBTS) is used as the HTL. The alignment of energy levels at the interfaces, particularly between the absorber and transport layers, has a vital impact on selecting charge extraction performance, minimizing recombination losses, and ultimately enhancing the total performance of the PSCs. Photogenerated electrons are collected by this arrangement at the back metallic electrode (Ni) and the front contact (Al). On the other hand, holes made in the conduction band of the ETL move in the direction of the HTL. The performance requirements of the device can be greatly impacted by any misalignment in the energy bands at the Cs_2SnBr_6/HTL and ETL/Cs_2SnBr_6 interfaces. The characteristics of the surfaces that affect interfacial recombination determine these consequences. The electrical properties of the ETL and HTL materials must therefore be precisely adjusted. To achieve effective hole extraction, the ionization energy of the HTL should be lower than that of Cs_2SnBr_6, while the electron affinity of the ETL must be higher than that of Cs_2SnBr_6. In the ideal models of Cs_2SnBr_6-based devices, the Fermi level is positioned close to the conduction band, as illustrated in Fig. 4(a), indicating n-type or degenerate semiconductor behavior.

Similarly, Fig. 5(a) demonstrates that when CdS is used as the ETL and CBTS serves as the HTL, the Fermi level remains near the conduction band. The configurations presented in Figs. 5(b) and 5(c), which utilize alternative HTLs such as P_3HT and CuO, respectively, both in combination with CdS as the ETL, also exhibit similar electronic characteristics, consistent with degenerate semiconductor behavior observed in Fig. 5(a). When the HTLs CBTS (1.90 eV), P_3HT (1.70 eV), and CuO (1.51 eV) are integrated into the device architecture with CdS, comparable photovoltaic performance is achieved, suggesting flexibility in HTL selection without significant compromise to efficiency. Figures 5(a), 5(b), and 5(c) are defined as Device-I (Al/FTO/CdS/Cs_2SnBr_6/CBTS/Ni), Device-II (Al/FTO/CdS/Cs_2SnBr_6/P_3HT/Ni), and Device-III

Optics EXPRESS

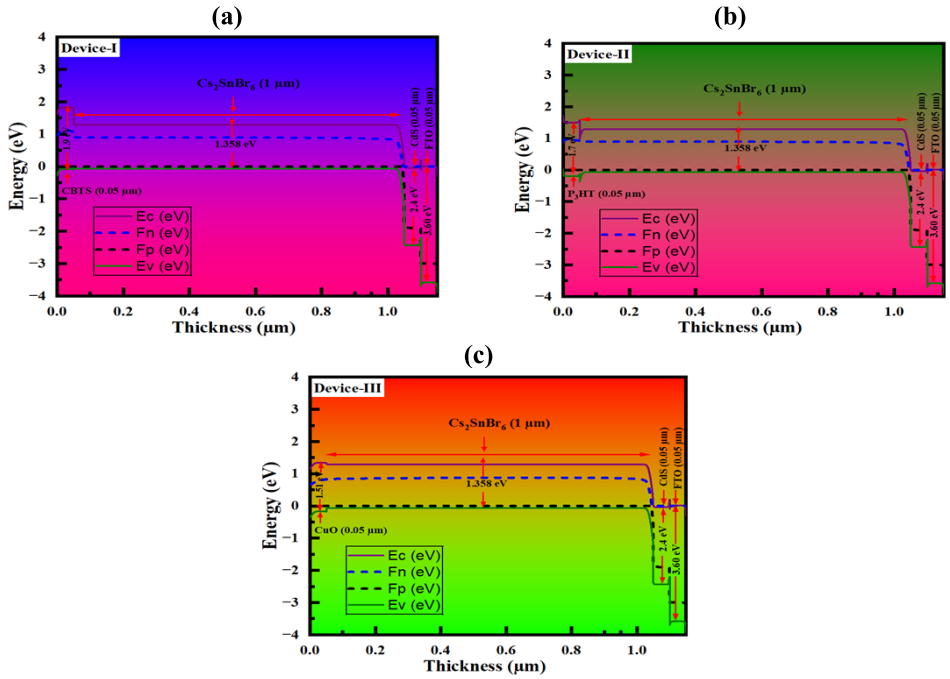

Fig. 5. Diagram of band with (a) CBTS, (b) P_3HT, (c) CuO.

(Al/FTO/CdS/Cs_2SnBr_6/CuO/Ni), respectively. Additionally, Figs. 5(a–c) illustrate the alignment of the valence energy band with the quasi-Fermi levels for holes (Fp) and electrons (Fn). In these configurations, Fp typically remains above the valence band maximum (Ev), while Fn aligns closely with the conduction band minimum (Ec), indicating a well-coordinated band structure that supports efficient charge separation and transport within the device.

3.4. Assessment of the thickness of absorber and HTL layers

The thickness of the absorber layer plays a crucial role in determining the performance of solar cells. A thicker absorber can capture more light, generating more electron-hole pairs and potentially increasing the short-circuit current. However, if the thickness exceeds the carrier diffusion length, many of these carriers may recombine before reaching the electrodes, reducing efficiency. This is especially important in materials like Cs_2SnBr_6, which typically have lower carrier mobility and shorter diffusion lengths. Additionally, overly thick layers can introduce more defects, increasing recombination losses. On the other hand, a very thin layer may not absorb sufficient light, limiting current generation. The depth of the perovskite level plays an important role in selecting the photovoltaic efficiency of PSCs [34,35]. To identify the ideal depth, simulations were conducted by gradually increasing the absorber layer from 200 nm to 2000nm. As shown in Fig. 6(a), the PCE increases significantly up to a thickness of 1000–1200 nm, after which it begins to plateau. At 1000 nm, the highest PCE values were observed: 32.60% for Device I, 30.51% for Device II, and 23.22% for Device III. Beyond this point, only marginal improvements were recorded. Figure 6(b) illustrates the variation in V_{OC}, where Devices II and III show a slight increase from 0.96 V to 0.97 V and 1.04 V to 1.042 V, respectively, up to 1000 nm, then stabilize. Device I, however, shows a slight decrease in V_{OC} up to 1000 nm, after which it remains constant at 1.11 V. Figure 6(c) shows that the J_{SC} also improves with thickness up to 1000 nm: Device I increases from 25.5 to 33.08 mA/cm^2, Device II from 26.51 to 32.98

Optics EXPRESS

mA/cm^2, while Device III decreases from 28.0 to 23.25 mA/cm^2. Beyond this thickness, the values level out. FF values, shown in Fig. 6(d), remain constant for Devices I and II at 80.82% and 86.25%, respectively, while Device III shows an increase from 85.85% to 86.93% up to 1000 nm. Additionally, Fig. 7 presents the impact of HTL thickness on device performance, using CBTS, P_3HT, and CuO as HTL materials.

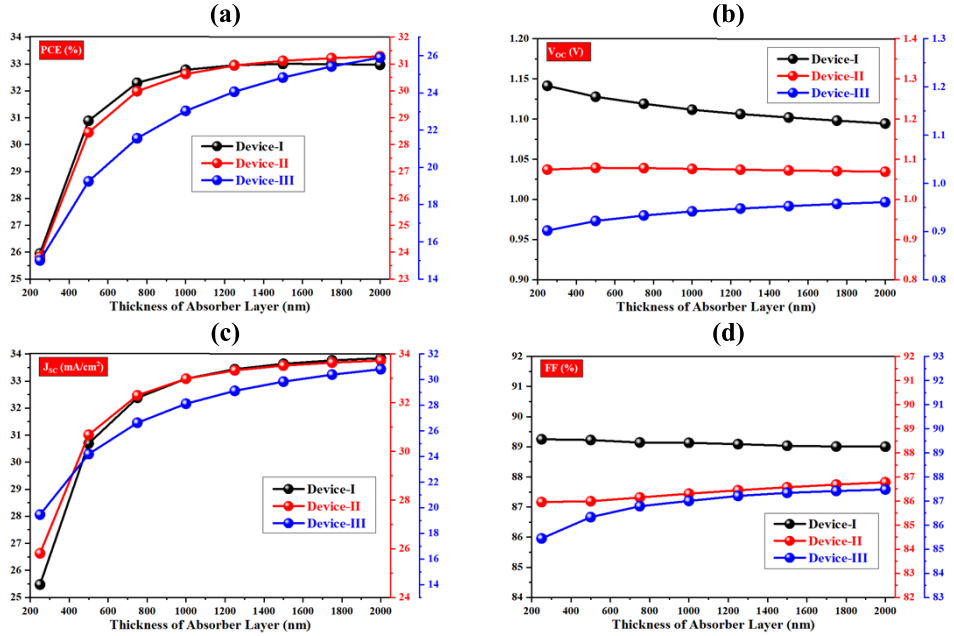

Fig. 6. Role of PV parameters taking into account the modification in thickness of absorber layer (a) PCE, (b) V_{OC}, (c) J_{SC}, and (d) FF.

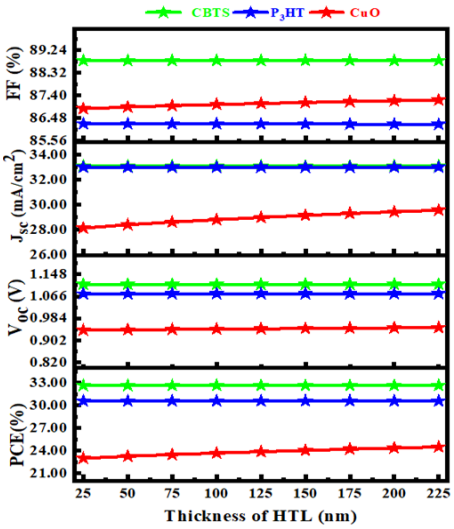

Fig. 7. Effect of PV parameters taking into account the modification in thickness of HTL layer for all device.

Optics EXPRESS

Adjusting the HTL thickness is essential not only for improving charge transport and reducing recombination losses but also for preventing direct contact between the absorber and the cathode, which could otherwise compromise device stability [12]. Among these materials, CBTS yielded the highest PCE and was thus selected for further optimization. The photovoltaic parameters across all HTL configurations remained relatively stable, with a slight increase in J_{SC} observed only in Device III (from 28.00 to 28.40 mA/cm^2). Other values, including V_{OC} (1.11 V, 1.075 V, 0.9416 V), FF (88.82%, 86.25%, 86.93%), and PCE (32.65%, 30.59%, 23.25%) for Devices I, II, and III, accordingly, showed minimal variation, while J_{SC} plateaued around 33 mA/cm^2 for models I and II. Overall, both PCE and FF improved with increasing HTL thickness due to enhanced charge extraction, although excessive thickness led to higher series resistance, slightly reducing efficiency. Based on these findings, the optimal absorber thickness was selected to be 1000 nm, and the optimal HTL depth using CBTS was 50 nm, which were adopted for further computational studies to ensure maximum device efficiency.

3.5. Consequences of doping and defect density for all devices

Figure 8 illustrates the role of N_A and N_t on the photovoltaic efficiency of a solar cell using a CBTS HTL, referred to as Device-I. To assess their influence on device efficiency, the analysis varied the absorber concentration of doping from 10^{13} to 10^{20} cm^{-3} while examining changes in N_t and N_A within a range of 10^{10} to 10^{16} cm^{-3} Lowering N_t improves PV performance by decreasing recombination losses and facilitating better charge transport. The PCE decreases from 39.70% to 20.40% as N_A and N_t fluctuate, highlighting the importance of optimizing these parameters. To achieve the highest PCE, the absorber requires a high N_A and a low N_t. N_t plays a direct role in device performance, as higher trap densities lead to enhanced recombination of charge within the perovskite level, thereby reducing the diffusion length of electron carriers [33]. The ideal PCE of 32.65%, as revealed in Fig. 8(a), is achieved with a doping concentration of 10^{18} cm^{-3} and an optimized N_t of 10^{18} cm^{-3}, balancing key photovoltaic parameters effectively. Figure 8(b) reveals that the V_{OC} varies significantly with changes in the Cs_2SnBr_6 doping concentration. However, a noticeable decline in V_{OC}, from 1.37 V to 0.778 V, is observed as N_t enhances. Similarly, the J_{SC}, shown in Fig. 8(c), levels off when the absorber doping concentration reaches 10^{18} cm^{-3} and N_t is maintained at or below 10^{14} cm^{-3}, peaking at 33.08 mA/cm^2. As both N_A and N_t are altered, J_{SC} decreases from 33.08 mA/cm^2 to 32.43 mA/cm^2, emphasizing the negative impact of N_t on charge carrier diffusion and increased recombination rates. The FF, depicted in Fig. 8(d), peaks at 88.82% at the ideal N_t value and sharply declines to 79.50% as N_t surpasses the optimal range, due to heightened carrier recombination. In a best-case situation, the device exhibits a V_{OC} of 1.11 V, an FF of 88.82%, and a J_{SC} of 33.08 mA/cm^2, demonstrating the critical role of doping concentration and trap density in optimizing the performance of Cs_2SnBr_6-based PSCs. The N_t within the absorber layer is crucial for influencing how well an SC works that employs a P_3HT HTL. The generation of photovoltaic (PV) energy occurs as a communication between light and the absorber.

Figure 9(a–d) demonstrates the influence of varying N_t, which ranges from 10^{10} to 10^{16} cm^{-3}, and different concentrations of absorber doping, from 10^{13} to 10^{20} 1/cm^3, on essential efficiency indicators like J_{SC}, PCE, V_{OC}, and FF. As the N_A increases from 10^{13} to 10^{20} 1/cm^3 and N_t escalates from 10^{10} to 10^{16} cm^{-3}, the device experiences a reduction in J_{SC} from 33.08 to 31.45 mA/cm^2, PCE from 29.9% to 18%, FF from 72% to 82%, and V_{OC} from 0.75 V to 1.09 V. The trends depicted in Fig. 9(a–d) indicate that ideal performance for J_{SC}, PCE, V_{OC}, and FF is attained when the absorber N_A exceeds 10^{18} cm^{-3} while maintaining a low N_t as much as possible. By carefully adjusting these parameters, the maximum PCE of 30.59% was achieved with a perovskite N_t of 10^{14} cm^{-3} and an N_A of 10^{18} cm^{-3}. In these ideal states, the solar cell produced a V_{OC} of 1.075 V, an FF of 86.25%, and a J_{SC} of 28.407 mA/cm^2. One critical factor influencing solar cell efficiency is the level of doping and the defect concentration within

Optics EXPRESS

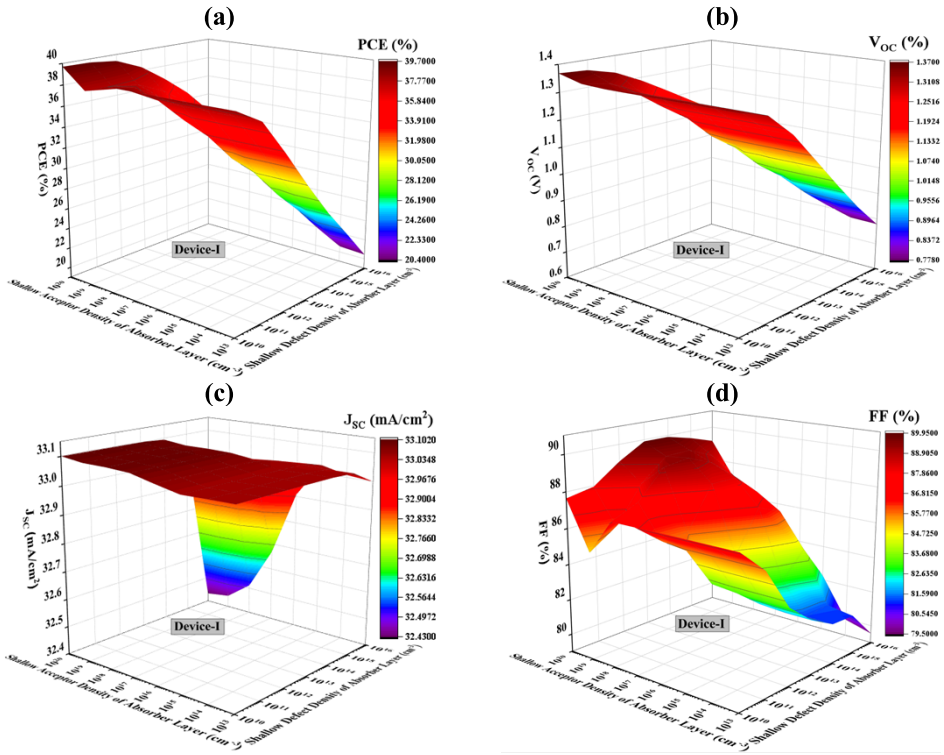

Fig. 8. An analysis of how variation in bulk defect density and doping of Cs_2SnBr_6 absorber influence photovoltaic performance (a) PCE, (b) V_{OC}, (c) J_{SC}, and (d)FF for Device-I.

the selected level. An increased defect density can lead to the formation of pinholes, which compromise the structural integrity of the layer, reduce device stability, and significantly enhance charge carrier recombination. As a result, overall device performance is adversely affected, underscoring the importance of careful control over both doping concentration and material quality during fabrication [36].

As depicted in Fig. 10(a-d) for Device-III, there is a clear trend where rising defect density correlates with a decline in all essential performance metrics. As the N_A increases from 10^{13} to 10^{20} 1/cm^3 and N_t escalates from 10^{10} to 10^{16} 1/cm^3, the device experiences a reduction in J_{SC} from 33.00 to 27 mA/cm^2, PCE from 25.79% to 20.43%, FF from 88.65% to 79.54%, and V_{OC} from 1.06 V to 0.78 V. At optimal N_A and N_t of 10^{18} and 10^{14} cm^{-3}, the SC demonstrates a V_{OC} of 0.94 V, a J_{SC} of 28.407 mA/cm^2, an FF of 86.93%, and a PCE of 23.25%. Previous studies have shown that increased defect density in the perovskite level significantly reduces the diffusion path length, thereby diminishing the overall efficiency of the device [37].

3.6. *Task of HTL doping concentration (N_A) and density of defect (N_t)*

Due to their significant influence on carrier extraction performance and the reduction of recombination losses, the presence of N_A and defects in the HTL plays a crucial role in enhancing the performance of solar cells [38,39]. For various HTLs, including CBTS, P_3HT, and CuO, the N_A and N_t were diverse within the ranges of 10^{13} to 10^{20} cm^{-3} and 10^{10} to 10^{16} 1/cm^3, respectively, while all other parameters were kept constant. The doping levels and defect densities corresponding to each device's N_A and N_t values are illustrated in Figs. 11(a) and 11(b). The enhanced performance of the solar cells increases the conductivity of the HTL, allowing it to

Optics EXPRESS

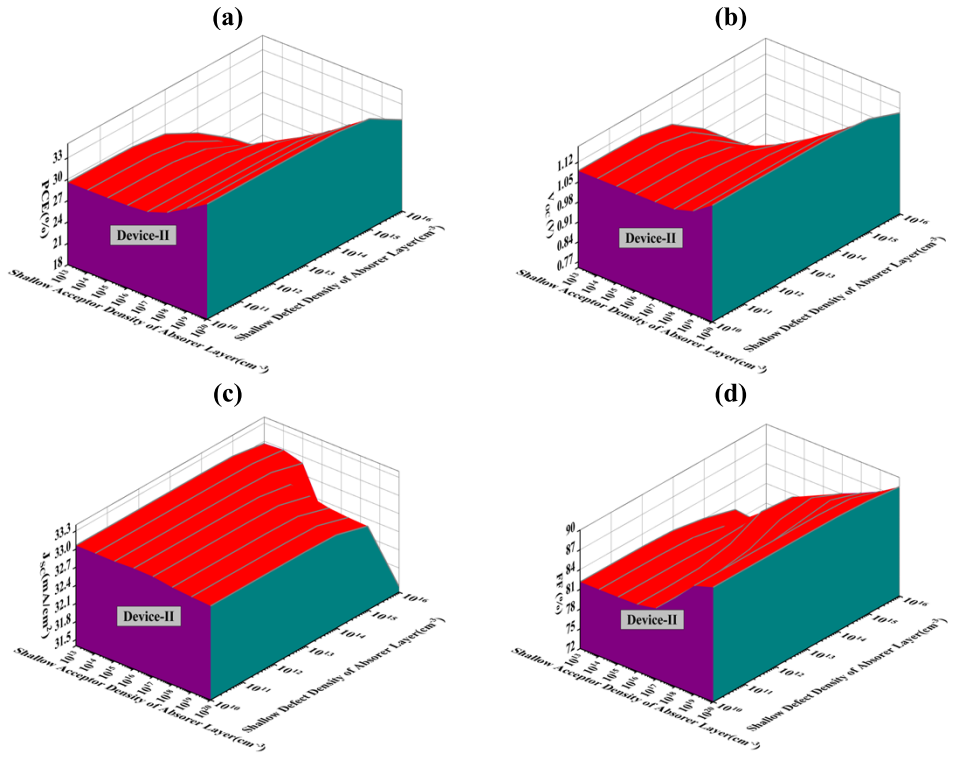

Fig. 9. An analysis of how variation in bulk defect density and doping of Cs_2SnBr_6 absorber influence photovoltaic performance (a) PCE, (b) V_{OC}, (c) J_{SC}, and (d) FF for Device-II.

support a higher hole concentration. This improvement facilitates more efficient hole transport toward the metal electrode, thereby reducing resistive losses [40].

Heavy doping of the HTL shifts the Fermi level closer to the valence band, enhancing energy level alignment with Cs_2SnBr_6 and improving hole collection efficiency. However, increasing the HTL N_A can lead to a reduction in V_{OC} due to the higher density of defects at the HTL–absorber interface. These defect-induced trap states promote carrier recombination, which reduces the quasi-Fermi level splitting and consequently lowers the V_{OC} [41]. However, in this simulation, all PV parameters remain constant even when the HTL N_A enhances up to $10^{18}\,cm^{-3}$. The V_{OC} for models I, II, and III are 1.111 V, 1.075 V, and 0.941 V, respectively. The corresponding J_{SC}'s are 33.084, 32.990, and 28.407 mA/cm^2. The FF for Devices I, II, and III are 88.82%, 86.25%, and 86.93%, respectively, while the PCE are 32.65%, 30.59%, and 23.25% (see Fig. 11(a)). Similarly, Fig. 11(b) confirms that the PV characteristics remain unchanged, with identical V_{OC}, J_{SC}, FF, and PCE values for models I, II, and III.

3.7. Augmentation of density of interface for defects

Interface defects, arising from structural imperfections during the fabrication of solar cells, significantly reduce efficiency by promoting charge carrier recombination [42]. Therefore, it is essential to assess their impact and refine manufacturing techniques to enhance effectiveness. This research looked into the effects of an impartial N_{tf} of $10^{10}\,cm^{-2}$ across several interfaces, specifically Device-I (CBTS/Cs_2SnBr_6, and Cs_2SnBr_6/CdS), Device-II (P_3HT/Cs_2SnBr_6, and Cs_2SnBr_6/CdS), and Device-III (CuO/Cs_2SnBr_6, and Cs_2SnBr_6/CdS) while keeping all solar cells' defect energy level at 0.6 eV, as shown in Fig. 12. The study evaluated how changing N_{tf}

Optics EXPRESS

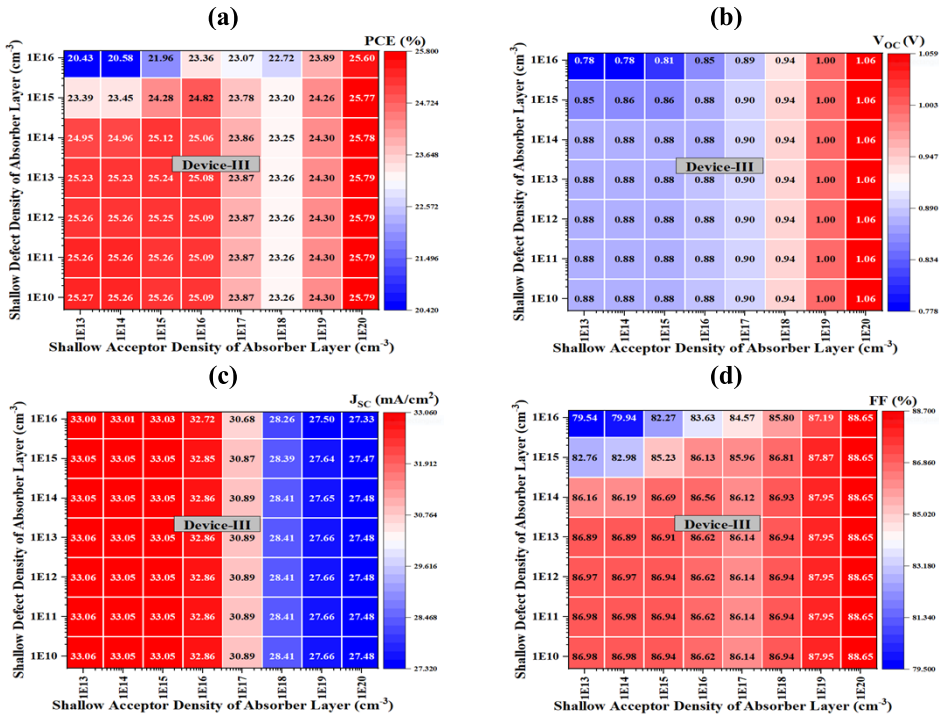

Fig. 10. An analysis of how variation in bulk density of defect and doping of Cs_2SnBr_6 perovskite influence photovoltaic performance (a) PCE, (b) V_{OC}, (c) J_{SC}, and (d)FF for Device-III.

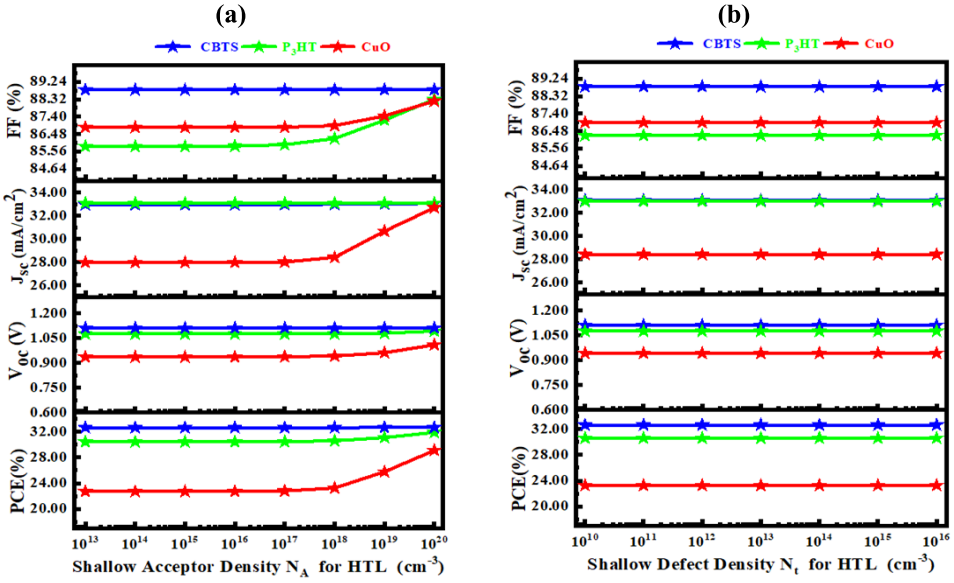

Fig. 11. (a) Doping (b) Defect density of with various HTLs.

from 10^8 to 10^{15} cm^{-2} influences solar cell efficiency. As outlined in Table 3, an increase in N_{tf} results in the formation of recombination centers that obstruct carrier transport, consequently

Optics EXPRESS

leading to declines in PV parameters. Furthermore, elevated densities of interface defects contribute to higher series resistance, which further compromises device performance [36]. N_{tf} is a critical factor influencing photovoltaic performance, particularly at the interfaces of Device-I (CBTS/Cs_2SnBr_6, and Cs_2SnBr_6/CdS), Device-II(P_3HT/Cs_2SnBr_6, and Cs_2SnBr_6/CdS), and Device-III (CuO/Cs_2SnBr_6, and Cs_2SnBr_6/CdS) .An increase in interface defect density leads to enhanced carrier recombination, thereby reducing the total efficiency of the devices [43].

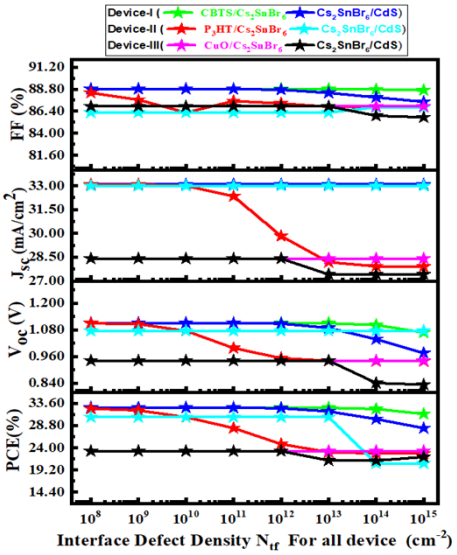

Fig. 12. Demonstrates how defects affect the photovoltaic characteristics at the interfaces.

Table 3. The impact of N_{tf} variation on PV specifications

Parameters/interface		V_{OC} (V)	J_{SC} (mA/cm^2)	FF (%)	PCE (%)
Device-I	CBTS/Cs_2SnBr_6	1.111-1.067	33.08-33.05	88.82-88.67	33.65-31.29
	Cs_2SnBr_6/CdS	1.111-0.975	33.09-33.08	88.82-87.41	32.65-28.21
Device-II	P_3HT/Cs_2SnBr_6	1.101-0.939	33.07-27.89	88.40-86.82	32.43-22.74
	Cs_2SnBr_6/CdS	1.075-1.074	32.98-32.97	86.24-86.82	30.59-20.59
Device-III	CuO/Cs_2SnBr_6	0.941-0.935	28.40-28.39	86.93-86.92	23.25-23.24
	Cs_2SnBr_6/CdS	0.941-0.833	28.40-27.41	86.93-85.73	23.25-21.99

3.8. Absorption coefficients of each layer

A material with a high absorption coefficient can absorb more incident light, leading to the generation of a greater number of electron-hole pairs and, consequently, a higher electrical output from the solar cell. This coefficient is wavelength-dependent: longer wavelengths tend to penetrate deeper into the material before being absorbed, while shorter, higher-energy wavelengths are typically absorbed near the surface. The light absorption coefficient is a key parameter in evaluating a material's qualification to harness light energy and plays a vital role in selecting PV cell efficiency. In photo cell applications, the first absorption peak indicates the wavelength spectrum over which a substance can effectively emit light, serving as an important metric in material selection and design [44]. Various materials, including Cs_2SnBr_6, P_3HT, CuO,

Optics EXPRESS

CdS, CBTS, and FTO, show different absorption coefficients at different wavelengths. Notably, Cs_2SnBr_6, P_3HT, CuO, CdS, and CBTS have elevated maxima of absorption near 200 nm, and FTO has 172.21 nm. These materials exhibit significant absorption elevations in visual and ultraviolet rays, with maximum absorption coefficients of 100000 cm^{-1} for FTO, 162695.764 cm^{-1} for P_3HT, 176235.187 cm^{-1} for CuO, 125828.67 cm^{-1} for CdS, 188824.068 cm^{-1} for Cs_2SnBr_6, and 150435.945 cm^{-1} for CBTS (see Fig. 13(a-d)).

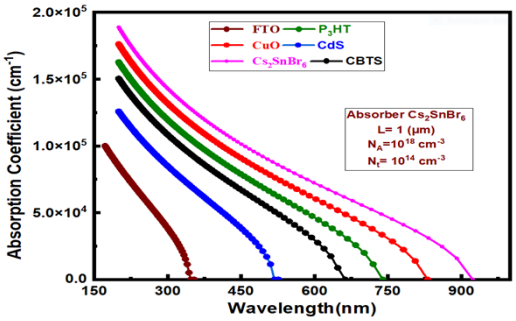

Fig. 13. All absorption coefficient

3.9. *Consequences of operating temperature*

Operating temperature significantly influences the efficiency of solar cells. Although the standard test condition is typically set at 300 K, solar cells often operate at higher temperatures under real-world conditions. As temperature increases, it affects various material properties, including bandgap, electrical resistance, charge carrier mobility, and carrier concentration, which collectively lead to a decline in key PV parameters such as efficiency, open-circuit voltage, and fill factor [45]. In this study, the SC's working temperature was set between 250 and 475 degrees Celsius. Temperature changes have distinct effects on the transport layers, which help convey charge carriers in the direction of the collective contact. This variability is attributed to differences in conductivity, specific heat, and density among the materials involved [46]. The effects of temperature on PCE, V_{OC}, J_{SC}, and FF are shown in Fig. 14. Similar patterns are shown for FF, J_{SC}, and PCE, and the decrease in V_{OC} becomes more pronounced as the temperature rises. Equation (8) is given to help clarify how temperature affects solar cell performance [47].

$$V_{OC} = \frac{E_A}{q} - \frac{nKT}{q} \ln\left(\frac{J_{00}}{J_{SC}}\right) \tag{8}$$

V_{OC} represents the open circuit voltage, E_A denotes the activation energy, the diode's ideality factor is denoted by n, and the Boltzmann constant by K; T indicates the temperature measured in Kelvin, J_{00} is the current pre-factor, and J_{SC} signifies the short circuit current. Equation (8) illustrates that as temperature rises, there is a notable decrease in V_{OC}. This observation implies that the rise in reverse saturation current contributes to the reduction of V_{OC} as temperature increases. Specifically, V_{OC}, FF, and PCE sharply drop from 0.89 V to 0.67 V, 88.64% to 77.96%, and 36.40% to 24.64%, respectively, with rising temperatures for optimal devices. J_{SC} remains constant at 46.00 mA/cm^2. Furthermore, it is observed that temperature and device performance have a linear connection, with lower temperatures leading to greater efficiency. Specifically, for the optimized devices, the V_{OC}, FF, and PCE decrease noticeably with increasing temperature from 1.116 V to 0.963 V, 90% to 83.71%, and 34.97% to 24.68%, respectively. In contrast, the J_{SC} remains constant at 33.084 mA/cm^2. Although higher efficiencies are achieved at lower temperatures, particularly at 250 K and 275 K, a temperature of 300 K is selected as the

Optics EXPRESS

optimal value, as it represents standard room temperature. Moreover, a nearly linear relationship is observed between temperature and device performance, with lower operating temperatures correlating with improved efficiency.

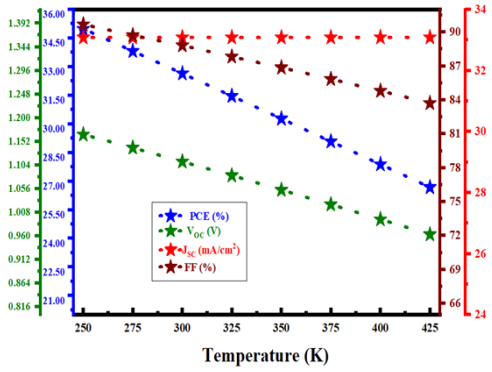

Fig. 14. Illustrates the impact of working temperature.

3.10. Analysis of JV and QE properties in Cs_2SnBr_6

Assessing the performance of SCs requires an understanding of current density, which quantifies the electric current generated per unit area and is a key indicator of device efficiency. Figure 15(a) presents the J-V characteristics of a device structure comprising Al/ITO/CdS/Cs_2SnBr_6/HTL/Ni, featuring three distinct HTLs, with a voltage range extending from 0 to 0.120 V. At the outset, all three configurations display comparable levels of photocurrent, maintaining a consistent response between 0.0 and 1.123 V. However, a noticeable reduction in photocurrent occurs in all PSCs within the 0.937-0.1.123 V voltage range. In the preliminary optimization phase, the HTLs made from CBTS, P_3HT, and CuO exhibited enhanced J-V performance, particularly in terms of J_{SC} and V_{OC}, when compared to those based on CBTS and P_3HT. Specifically, the PSCs utilizing Devices I, II, and III achieved a J_{SC} of approximately 33.084 mA/cm^2. Furthermore, when the applied voltage rose, the photocurrent in all designs significantly decreased.

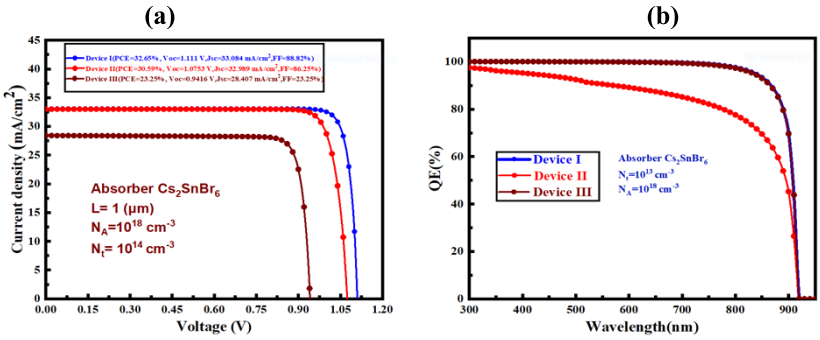

Fig. 15. Represents the (a) J-V ordinary sloped and (b) Quantum Efficiency curve for Cs_2SnBr_6.

Figure 15(b) depicts the relationship between quantum efficiency (QE) and wavelength for PSCs that employ models I, II, and III, encompassing the wavelength range of 300-1000 nm. The QE spectra corresponding to each configuration are shown in Fig. 15(b). At a spectrum wavelength of 300 nm, PSCs utilizing CBTS, P_3HT, and CuO HTLs achieved a peak QE of 100%

Optics EXPRESS

and a minimum at 940 nm. The decline in QE observed in most solar cells is primarily attributed to recombination processes that hinder charge carriers from reaching the external circuit. Various factors, including modifications to the front surface that affect carrier collection probability, also play a role in influencing QE. Furthermore, at longer wavelengths, the absorption of free carriers in heavily doped front surface layers can contribute to a further reduction in QE [48]. All device designs exhibited a gradual decline in quantum efficiency (QE) with increasing wavelength after reaching their peak values. This trend is due to the reduced absorption of longer-wavelength photons. In general, increasing the absorber layer thickness enhances QE, as a fatter absorber can capture more incident photons, leading to greater carrier generation [49].

4. Selecting optimal structure and a comparison between the results of SCAPS-1D and earlier studies

We have investigated Cs_2SnBr_6-based solar cells and observed that the initial use of CdS as ETL led to suboptimal device performance. Even so, persistent investigation has led to an important finding: a highest performance of 29.22% was displayed previously in the current year [26]. The study identified a configuration that achieved an impressive maximum efficiency of 32.65%, as illustrated in Fig. 16. This performance was made possible through the use of a CdS ETL and a CBTS HTL, resulting in a J_{SC} of 33.084 mA/cm^2, an FF of 82.82%, and a V_{OC} of 1.111 V. To enhance the reliability and accuracy of simulation results, as summarized in Table 4, future experimental investigations should adopt a comprehensive approach that encompasses material synthesis, characterization, device fabrication, performance evaluation, and stability testing.

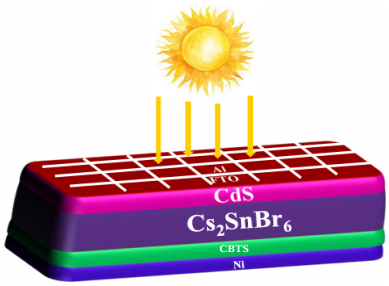

Fig. 16. The advanced structure of the optimized framework

5. Conclusion

This study presented the modeling and analysis of a lead-free PSC based on a Cs_2SnBr_6 absorber. Among the evaluated configurations, the Al/FTO/CdS/Cs_2SnBr_6/CBTS/Ni architecture achieved the highest simulated performance, with a PCE of 32.65%, a J_{SC} of 33.084 mA/cm^2, a V_{OC} of 1.111 V, and an FF of 88.82%. While the simulated results reveal the strong potential of Cs_2SnBr_6 based PSCs, experimental validation is essential to confirm their practical viability. Key challenges include interfacial instability, fabrication complexity, and limited data on long-term operational stability. Environmental factors such as humidity and thermal cycling also need thorough investigation. Future research should prioritize the synthesis of high-purity Cs_2SnBr_6, interface optimization, and scalable fabrication techniques. Despite these hurdles, the fully inorganic, lead-free nature and high efficiency of Cs_2SnBr_6 highlight its promise for sustainable, next-generation solar energy technologies.

Optics EXPRESS

Table 4. Compares the PV performance indicates discovered in this investigation to those discovered in earlier double absorber designs that have been documented in the literature

Model	V_{OC} (V)	J_{SC} (mA/cm^2)	FF (%)	PCE (%)	Ref.
Device-I	**1.11**	**33.084**	**88.82**	**32.65**	This Work*
Device-II	**1.075**	**32.989**	**86.25**	**30.59**	This Work*
Device-III	**0.942**	**28.407**	**86.93**	**23.25**	This Work*
FTO/SnS_2/$RbSnBr_3$	0.98	47.21	77.67	29.79	[29]
FTO/SnS_2/$RbSnI_3$	0.83	51.83	81.44	26.38	[29]
FTO/SnS_2/$RbSnCl_3$	1.24	36.55	87.31	32.23	[29]
TiO_2/$CsPbI_3$/CBTS	0.99	21.07	85.21	17.9%	[50]
CuSCN/$CsGeI_3$/C_{60}	1.0169	19.653	88.13	17.61	[51]
SnS_2/Ca_3NCl_3/MoO_3	1.36	22.89	90.36	28.13	[52]
CuSCN/$FASnI_3$/Zn	1.0859	28.12	84.96	25.94	[32]
CuI//$KSnI_3$/ZnO/FTO	1.44	17.06	85.24	20.99	[53]
WS_2/$Cs_4CuSb_2Cl_{12}$/$CuSbS_2$	1.16	29.27	83.33	23.10	[54]
ZnMgO/$CsSnI_3$/GO	0.62	35.61	78.21	17.37	[55]
FTO/TiO_2/ Cs_2SnBr_6	1.02	32.27	88.38	29.22	[26]
FTO/TiO_2/Na_2SnBr_6	0.77	42.69	81.85	29.51	[26]

Funding. King Khalid University (RGP2/218/46).

Acknowledgement. The authors extend their appreciation to the Deanship of Research and Graduate Studies at King Khalid University for funding this work through Large Research Project under grant number RGP2/218/46.

Disclosures. The authors have no conflicts of interest.

Author Contributions. Md. Selim Reza, and Avijit Ghosh: Conceptualization, methodology, software, validation, formal analysis, visualization, investigation, data curation, supervision, writing—original draft, and review and editing.

Yedluri Anil Kumar, Khorshed Alam, Md Al Imran, Md Mahfuzur Rahman, Nasser S. Awwad, and Hala A. Ibrahium: Software, validation, formal analysis, writing—original draft, and review and editing.

Ethical approval. All the authors declare that the manuscript does not have studies on human subjects, human data or tissue, or animals.

Data availability. Data will be made available on reasonable request.

References

1. M. E. Karim, R. Karim, M. T. Islam, *et al.*, "Renewable energy for sustainable growth and development: an evaluation of law and policy of Bangladesh," Sustainability **11**(20), 5774 (2019).
2. R. Yao, S. Ji, T. Zhou, *et al.*, "Self-energy correction and numerical simulation for efficient lead-free double perovskite solar cells," Phys. Chem. Chem. Phys. **26**(6), 5253–5261 (2024).
3. K. Liang, L. Huang, T. Wang, *et al.*, "Rational design of formamidine tin-based perovskite solar cell with 30% potential efficiency via 1-D device simulation," Phys. Chem. Chem. Phys. **25**(13), 9413–9427 (2023).
4. H. Shirai, T. Ariyoshi, J. Hanna, *et al.*, "Stability and hole-transport in a-Si:H prepared by 'Chemical Annealing,'," J. Non. Cryst. Solids **137-138**, 693–696 (1991).
5. M. K. A. Mohammed, S. M. Abdalhadi, A. Kumar, *et al.*, "Designing a novel hole-transporting layer for FAPbI 3-based perovskite solar cells," Energy Fuels **37**(24), 19870–19881 (2023).
6. S. Bhattarai, M. K. Hossain, R. Pandey, *et al.*, "Perovskite solar cells with dual light absorber layers for performance efficiency exceeding 30%," Energy Fuels **37**(14), 10631–10641 (2023).
7. S. B. Turgut and B. Gultekin, "Improving power conversion efficiency by light-assisted annealing of triple cation perovskite layer in solar cell applications," Sol. Energy **234**, 1–8 (2022).
8. M. A. Green, "Third generation photovoltaics: Ultra-high conversion efficiency at low cost," Prog. Photovoltaics Res. Appl. **9**(2), 123–135 (2001).
9. L. Moulaoui, O. Bajjou, A. Najim, *et al.*, "Numerical simulation of the NiO as hole transport layer in CH 3 NH 3 PbBr 3 perovskite based-solar cell using SCAPS-1D," in *2022 2nd International Conference on Innovative Research in Applied Science, Engineering and Technology (IRASET)*, Mar. 2022, pp. 1–7.
10. M. S. Uddin, R. Hosen, S. Sikder, *et al.*, "Photovoltaic performance enhancement of Al/ZnO:Al/i-ZnO/CdS /CIGS/Pt solar cell using SCAPS-1D software," Next Energy **2**, 100080 (2024).

Optics EXPRESS

11. M. K. Hossain, O. Alsalman, S. Rana, *et al.*, "Enhancing efficiency and performance of Cs2TiI6-based perovskite solar cells through extensive optimization: A numerical approach," Inorg. Chem. Commun. **168**, 112964 (2024).
12. U. Mandadapu, "Simulation and analysis of lead based perovskite solar cell using SCAPS-1D," Indian J. Sci. Technol. **10**(1), 1–8 (2017).
13. A. Kumar, A. Kumar, C.-P. M.M.S., *et al.*, "Lead toxicity: health hazards, influence on food chain, and sustainable remediation approaches," Int. J. Environ. Res. Public Health **17**(7), 2179 (2020).
14. M. A. Assi, M. N. M. Hezmee, A. W. Haron, *et al.*, "The detrimental effects of lead on human and animal health," Vet. World **9**(6), 660–671 (2016).
15. M. Wang, W. Wang, B. Ma, *et al.*, "Lead-free perovskite materials for solar cells," Nano-Micro Lett. **13**(1), 62 (2021).
16. A. K. Chauhan, P. Kumar, and S. N. Sharma, "An improvement in un-Encapsulated perovskite solar cell's environmental stability via introduction of an electrode interface layer," Mater. Technol. **37**(14), 3079–3088 (2022).
17. M. Chen, M.-G. Ju, H. F. Garces, *et al.*, "Highly stable and efficient all-inorganic lead-free perovskite solar cells with native-oxide passivation," Nat. Commun. **10**(1), 16 (2019).
18. M. Chen, G. Kapil, L. Wang, *et al.*, "High performance wide bandgap Lead-free perovskite solar cells by monolayer engineering," Chem. Eng. J. **436**, 135196 (2022).
19. M. K. Hossain, G. F. I. Toki, A. Kuddus, *et al.*, "An extensive study on multiple ETL and HTL layers to design and simulation of high-performance lead-free CsSnCl3-based perovskite solar cells," Sci. Rep. **13**(1), 2521 (2023).
20. J. Zhou, J. Luo, X. Rong, *et al.*, "Lead-free perovskite derivative Cs 2 SnCl 6− x Br x single crystals for narrowband photodetectors," Adv. Opt. Mater. **7**(10), 201900139 (2019).
21. G. Yuan, S. Huang, J. Niu, *et al.*, "Compressibility of Cs 2 SnBr 6 by X-ray diffraction and Raman spectroscopy," Solid State Commun. **275**, 68–72 (2018).
22. M. G. Brik and I. V. Kityk, "Modeling of lattice constant and their relations with ionic radii and electronegativity of constituting ions of A2XY6 cubic crystals (A=K, Cs, Rb, Tl; X=tetravalent cation, Y=F, Cl, Br, I)," J. Phys. Chem. Solids **72**(11), 1256–1260 (2011).
23. Md. S. Reza, Md. F. Rahman, A. Kuddus, *et al.*, "Boosting efficiency above 28% using effective charge transport layer with Sr 3 SbI 3 based novel inorganic perovskite," RSC Adv. **13**(45), 31330–31345 (2023).
24. A. Ait Abdelkadir and M. Sahal, "Theoretical development of the CZTS thin-film solar cell by SCAPS-1D software based on experimental work," Mater. Sci. Eng. B **296**, 116710 (2023).
25. R. K. Yadav, P. S. Pawar, R. Nandi, *et al.*, "A qualitative study of SnSe thin film solar cells using SCAPS 1D and comparison with experimental results: A pathway towards 22.69% efficiency," Sol. Energy Mater. Sol. Cells **244**, 111835 (2022).
26. Md. F. Rahman, T. Al Galib, Md. A. Rahman, *et al.*, "Achieving efficiency above 30% with new inorganic cubic perovskites X 2 SnBr 6 (X = Cs, Rb, K, Na) via DFT and SCAPS-1D," Phys. Chem. Chem. Phys. **27**(2), 1155–1170 (2025).
27. M. Burgelman, K. Decock, S. Khelifi, *et al.*, "Advanced electrical simulation of thin film solar cells," Thin Solid Films **535**(1), 296–301 (2013).
28. S. Tariq Jan and M. Noman, "Influence of layer thickness, defect density, doping concentration, interface defects, work function, working temperature and reflecting coating on lead-free perovskite solar cell," Sol. Energy **237**, 29–43 (2022).
29. M. Harun-Or-Rashid, M. F. Rahman, M. Amami, *et al.*, "Exploring new lead-free halide perovskites RbSnM3 (M = I, Br, Cl) and achieving power conversion efficiency > 32%," J. Phys. Chem. Solids **197**, 112437 (2025).
30. M. A. Rahman, "Performance analysis of WSe2-based bifacial solar cells with different electron transport and hole transport materials by SCAPS-1D," Heliyon **8**(6), e09800 (2022).
31. X. Li, J. Yang, Q. Jiang, *et al.*, "Low-temperature solution-processed ZnSe electron transport layer for efficient planar perovskite solar cells with negligible hysteresis and improved photostability," ACS Nano **12**(6), 5605–5614 (2018).
32. A. Tara, V. Bharti, S. Sharma, *et al.*, "Device simulation of FASnI3 based perovskite solar cell with Zn(O0.3, S0.7) as electron transport layer using SCAPS-1D," Opt. Mater. **119**, 111362 (2021).
33. K. K. Mamta, V. N. Maurya, and Singh, "Influence of buffer layers on antimony selenide based solar cell," Opt. Mater. **126**, 112240 (2022).
34. F. Kherrat, L. Dehimi, H. Bencherif, *et al.*, "Performance enhancement of eco-friendly Cs3Sb2I9-based perovskite solar cell employing Nb2O5 and CuI as efficient charge transport layers," Micro Nanostruct. **183**, 207676 (2023).
35. M. Mammeri, L. Dehimi, H. Bencherif, *et al.*, "Paths towards high perovskite solar cells stability using machine learning techniques," Sol. Energy **249**, 651–660 (2023).
36. Z. Gu, F. Chen, X. Zhang, *et al.*, "Novel planar heterostructure perovskite solar cells with CdS nanorods array as electron transport layer," Sol. Energy Mater. Sol. Cells **140**, 396–404 (2015).
37. L. Et-taya, T. Ouslimane, and A. Benami, "Numerical analysis of earth-abundant Cu2ZnSn(SxSe1-x)4 solar cells based on spectroscopic ellipsometry results by using SCAPS-1D," Sol. Energy **201**, 827–835 (2020).
38. F. B. Sumona, M. Kashif, J. Madan, *et al.*, "Optimization of lead-free KSnI3 perovskite solar cell by numerical simulation with enhanced efficiency of 20.34%," J. Opt. 5 (2024).
39. S. A. Moiz and A. N. M. Alahmadi, "Design of dopant and lead-free novel perovskite solar cell for 16.85% Efficiency," Polymers **13**(13), 2110 (2021).
40. E. Danladi, P. R. Jubu, A. M. Tighezza, *et al.*, "Highly efficient, hole transport layer (HTL)-free perovskite solar cell based on lithium-doped electron transport layer by device simulation," Emergent Mater. **6**(6), 1779–1795 (2023).

Optics EXPRESS

41. E. Danladi, M. Kashif, A. Ichoja, *et al.*, "Modeling of a Sn-based HTM-free perovskite solar cell using a one-dimensional solar cell capacitance simulator tool," Trans. Tianjin Univ. **29**(1), 62–72 (2023).
42. J. Cerdà, J. Arbiol, R. Diaz, *et al.*, "Synthesis of perovskite-type BaSnO3 particles obtained by a new simple wet chemical route based on a sol–gel process," Mater. Lett. **56**(3), 131–136 (2002).
43. C. Chen, D. C. Bobela, Y. Yang, *et al.*, "Characterization of basic physical properties of Sb2Se3 and its relevance for photovoltaics," Front. Optoelectron. **10**(1), 18–30 (2017).
44. P. Singh and N. M. Ravindra, "Analysis of series and shunt resistance in silicon solar cells using single and double exponential models," Emerg. Mater. Res. **1**(1), 33–38 (2012).
45. I. Alam and M. A. Ashraf, "Effect of different device parameters on tin-based perovskite solar cell coupled with In 2 S 3 electron transport layer and CuSCN and Spiro-OMeTAD alternative hole transport layers for high-efficiency performance," Energy Sources, Part A **46**(1), 17080–17096 (2024).
46. A. D. Adewoyin, M. A. Olopade, O. O. Oyebola, *et al.*, "Development of CZTGS/CZTS tandem thin film solar cell using SCAPS-1D," Optik **176**, 132–142 (2019).
47. P. Roy, N. K. Sinha, and A. Khare, "An investigation on the impact of temperature variation over the performance of tin-based perovskite solar cell: A numerical simulation approach," Mater. Today Proc. **39**, 2022–2026 (2021).
48. M. K. Hossain, M. K. A. Mohammed, R. Pandey, *et al.*, "Numerical analysis in DFT and SCAPS-1D on the influence of different charge transport layers of CsPbBr 3 perovskite solar cells," Energy Fuels **37**(8), 6078–6098 (2023).
49. K. K. Mamta, V. N. Maurya, and Singh, "Sb2Se3/CZTS dual absorber layer based solar cell with 36.32% efficiency: A numerical simulation," J. Sci. Adv. Mater. Devices **7**(2), 100445 (2022).
50. M. K. Hossain, M. H. K. Rubel, G. F. I. Toki, *et al.*, "Effect of various electron and hole transport layers on the performance of CsPbI 3 -based perovskite solar cells: a numerical investigation in DFT, SCAPS-1D, and wxAMPS frameworks," ACS Omega **7**(47), 43210–43230 (2022).
51. W. Ahmad, M. Noman, S. Tariq Jan, *et al.*, "Performance analysis and optimization of inverted inorganic CsGeI 3 perovskite cells with carbon/copper charge transport materials using SCAPS-1D," R. Soc. Open Sci. **10**(3), 221127 (2023).
52. Md. Shamim Reza, A. Ghosh, A. Kalam Azad, *et al.*, "Boosting the effectiveness of a cutting-edge Ca3NCl3 perovskite solar cell by fine-tuning the hole transport layer," Mater. Sci. Eng. B **309**, 117656 (2024).
53. F. B. Sumona, M. Kashif, E. Danladi, *et al.*, "Optimization of perovskite-KSnI 3 solar cell by using different hole and electron transport layers: a numerical SCAPS-1D simulation," Energy Fuels **37**(23), 19207–19219 (2023).
54. H. Karmaker, A. Siddique, B. K. Das, *et al.*, "Modeling and performance investigation of novel inorganic Cs4CuSb2Cl12 nanocrystal perovskite solar cell using SCAPS-1D," Results Eng. **22**, 102106 (2024).
55. K. Afridi, M. Noman, and S. T. Jan, "Evaluating the influence of novel charge transport materials on the photovoltaic properties of MASnI 3 solar cells through SCAPS-1D modelling," R. Soc. Open Sci. **11**(1), 231202 (2024).